Materials & Design 226 (2023) 111660

Contents lists available at ScienceDirect

Materials & Design

journal homepage: www.elsevier.com/locate/matdes

Fabrication of high-aspect-ratio and hierarchical micro/nanostructure arrays by a novel piezoelectrically actuated cutting system

Hanheng Du [a], Zhiwei Zhu [b], Zuankai Wang [c], Suet To [a,*]

[a] State Key Laboratory of Ultra-precision Machining Technology, Department of Industrial and Systems Engineering, The Hong Kong Polytechnic University, Hong Kong, China
[b] School of Mechanical Engineering, Nanjing University of Science and Technology, Nanjing, China
[c] Department of Mechanical Engineering, The Hong Kong Polytechnic University, Hong Kong, China

HIGHLIGHTS

- A piezoelectrically actuated cutting system was designed.
- A performance test platform was built.
- Various micro/nanostructure arrays were fabricated.
- Micro/nanostructure arrays improved the corrosion resistance.

GRAPHICAL ABSTRACT

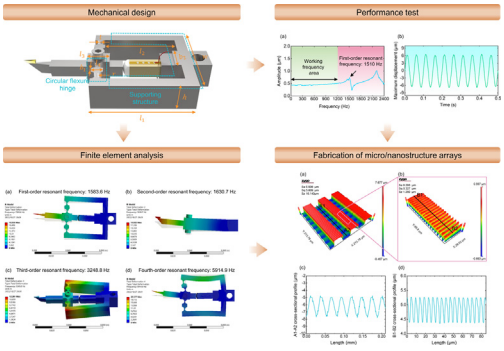

ARTICLE INFO

Article history:
Received 4 December 2022
Revised 23 January 2023
Accepted 24 January 2023
Available online 26 January 2023

Keywords:
Micro/nanostructure array
Ultraprecision machining
Piezoelectric actuator
Cutting system
Vibration-assisted machining
Finite element analysis

ABSTRACT

Micro/nanostructure arrays have been broadly applied in numerous industrial fields, such as optics, antibacterial fields, and anti-corrosion. However, the highly efficient fabrication of micro/nanostructure arrays, especially the high-aspect-ratio and hierarchical micro/nanostructure arrays, remains a challenge. Motivated by this, the study designs a novel piezoelectrically actuated (PA) cutting system for fabricating this kind of micro/nanostructure array. First, the mechanical structure of the PA cutting system is designed based on the circular flexure hinge. Then, a finite element model is established to analyze its resonant frequencies and mode shapes. Next, to determine the working performances of the PA cutting system, a performance test platform is built. Finally, various micro/nanostructure arrays with two features of the high-aspect-ratio and the multilayer are fabricated, demonstrating the effectiveness and flexibility of the PA cutting system. Besides, the function of machined micro/nanostructure arrays about the corrosion property was investigated. This study provides a new approach for fabricating high-aspect-ratio and hierarchical micro/nanostructure arrays, which can be applied in industrial manufacturing and corrosion protection fields.

1. Introduction

Micro/nanostructure arrays are drawing increasing interest because of their outstanding properties in optics, superhydrophobicity, self-cleaning, anti-corrosion, etc. For example, nano-tree arrays can realize continual fog harvesting. The harvesting effi-

* Corresponding author.
E-mail address: sandy.to@polyu.edu.hk (S. To).

https://doi.org/10.1016/j.matdes.2023.111660
0264-1275/

ciency is higher by 85 % than the original surface [1]. The micro-pillar array can enhance the electrical output performances of triboelectric nanogenerators by increasing the contact area of triboelectric materials, providing a 184.6 μW/cm^2 power density [2]. The micro-dimple array can reduce friction by 80 % in comparison with untextured surfaces [3]. The heat transfer is dramatically enhanced by using the micro-channel in the heat exchangers [4].

But how to generate these functional micro/nanostructure arrays has become a hot topic. Lithography and two-photon polymerization are popular fabrication processes. They fabricate micro-groove arrays [5], mushroom-like pillar arrays [6], and micro-needle [7], but the expensive equipment, specific material, and laborious steps limit the large-area fabrication of micro/nanostructure arrays. The beam-assisted machining process is another fabrication method that utilizes the focused ion beam or laser beam to generate micro/nanostructure arrays. It includes focused ion beam milling [8] and laser beam machining [9], but the low surface quality and low fabrication efficiency influence their wide applications in industrial production.

Ultraprecision cutting using the single-crystal-diamond (SCD) cutting tool is a promising machining method due to its low cost, good surface quality, and applicability to numerous engineering materials [10]. According to the relative motion relationship of the workpiece and cutting tool, it can be divided into fly cutting, diamond milling, single-point diamond turning (SPDT), and vibration-assisted diamond machining. In fly cutting and diamond milling, the SCD cutting tool is installed on the spindle of the machine tool while in diamond turning and vibration-assisted diamond machining the workpiece is mounted on the spindle. Zhu et al. [11] applied the fly cutting process to machine micro-pyramid arrays and sinusoidal grid microstructure arrays. Zhou et al. [12] utilized diamond milling to create micro-lens arrays on the surface of a nickel-phosphorous plated mold. The surface roughness of generated micro-lens arrays can reach 7.9 nm. But the non-continuous contact between the cutting edge of the SCD cutting tool and the workpiece influences fabrication efficiencies of the fly cutting and diamond milling. The SPDT and vibration-assisted diamond machining have continuous contact during fabricating of micro/nanostructure arrays. Meier [13] applied the SPDT method to fabricate diffractive microstructures and explored the influences of different material properties on cutting forces, chip formation, and surface finish. By designing the specific cutting paths, single-point diamond turning can be used to fabricate some simple microstructure arrays. In order to fabricate more complex micro/nanostructure arrays, vibration-assisted diamond machining is fast developing recently. In vibration-assisted diamond machining, a higher-order motion (vibration motion) is superimposed on the cutting tool [14–16]. Combining with the motions of the rotational axis and the linear axis of the ultraprecision lathe, periodical cutting trajectories are generated. These synchronization motions between the workpiece and the cutting tool help the diamond cutting tool to remove the surface materials of the workpiece and fabricate the micro/nanostructure arrays. Suzuki et al. [17] designed an elliptical vibration cutting device and developed a control system to realize the fabrication of micro-grooves. The sinusoidal-shaped, zigzag-shaped, and ramp-shaped micro-groove arrays were fabricated on the surfaces of hardened steel. Guo et al.[18] designed an ultrasonic vibration device, which was inspired by an ultrasonic motor, to generate elliptical vibration trajectories. Micro-dimple arrays were generated on the aluminum alloy surfaces by using this device, which operated at 28 kHz.

The above devices have a common feature: they only operate at a fixed frequency (namely, the resonant frequency), which influences the fabrication flexibility. The non-resonant vibration cutting devices can solve this problem, which is also named the fast-tool-servo device (cutting system). They are generally driven by the piezoelectric actuator or electromagnetic actuator. In our previous studies, different fast-tool-servo cutting systems were developed to solve the small stroke, small stiffness, or low working frequency [19–21]. But the high-aspect-ratio and hierarchical micro/nanostructure arrays still cannot be fabricated by using the existing cutting systems, due to the limitations of the arc-shaped SCD cutting tool that is widely used in the existing cutting systems.

To solve the above problems, this study designs a novel piezoelectrically actuated (PA) cutting system for generating high-aspect-ratio and hierarchical micro/nanostructure arrays on metal surfaces, which can work at 1200 Hz. In Section 2, the mechanical structure and working principle of the PA cutting system are illustrated. Section 3 analyzes resonant frequencies and mode shapes using finite element analysis. Section 4 describes the performance test platform and fabrication experimental setup. Section 5 discusses the working performances of the PA cutting system, characterization of micro/nanostructure arrays, and corresponding corrosion properties of micro/nanostructure arrays. Finally, Section 6 concludes this study.

2. Mechanical design of the piezoelectrically actuated cutting system

The aspect ratio is the value of the height of micro/nanostructure arrays over the width. The high-aspect-ratio micro/nanostructure arrays are of specific interest in many fields, such as sensor [22], wetting [23], and microfluidics [24]. In general, the high aspect ratio increases the challenge of fabricating them [25,26]. From the scanning electron microscope image of the arc-shaped SCD cutting tool, it has nearly no chance to fabricate the high-aspect-ratio micro/nanostructure arrays, as described in Fig. 1(a). Because when increasing the depth-of-cutting, the width of the micro/nanostructure arrays (perpendicular to the depth-of-cutting direction) dramatically increase because of the existence of the arc-shaped cutting edge. But the trapezoid-shaped SCD cutting tool provides the chance of fabricating high-aspect-ratio micro/nanostructure arrays because it has a very narrow cutting edge, as described in Fig. 1(b).

In this study, a piezoelectric actuator is chosen to be a vibration source. Therefore, the next problem is how to add the vibration motion from the piezoelectric actuator into the trapezoid-shaped SCD cutting tool. It is because if the hierarchical micro/nanostructure arrays are fabricated by using the one-step process, the cutting tool has to have higher-order vibration motions. There are mainly-two types of flexible hinges that help to transfer the vibration motion of the piezoelectric actuator into the trapezoid-shaped SCD cutting tool. They are the right-angle flexure hinge [27] and circular flexure hinge [28], as presented in Fig. 2(a) and (d). The first-order resonant frequency of the flexure hinge influences the working frequency of the cutting system. The stiffness influences the stability of the cutting system. In general, the high first-order resonant frequency represents the high working frequency. The larger stiffness represents the high resistance to external disturbances. These two indicators are chosen to evaluate the performance of flexure hinges.

A finite element simulation software "ANSYS 19.0" was used to analyze the above two indicators. The simulated results are shown in Fig. 2(b) and (e), which shows that the first-order resonant frequency of the circular flexure hinge (21291 Hz) is far higher than that of the right-angle flexure hinge (6328.7 Hz). For the stiffness, static structural analysis was conducted by inputting an external disturbance force of 1 N, as presented in Fig. 2(c) and (f). The stiffness of the circular flexure hinge (31.02 N/μm) is also far bigger than that of the right-angle flexure hinge (1.71 N/μm). Therefore, it can be concluded that the circular flexure hinge has better per-

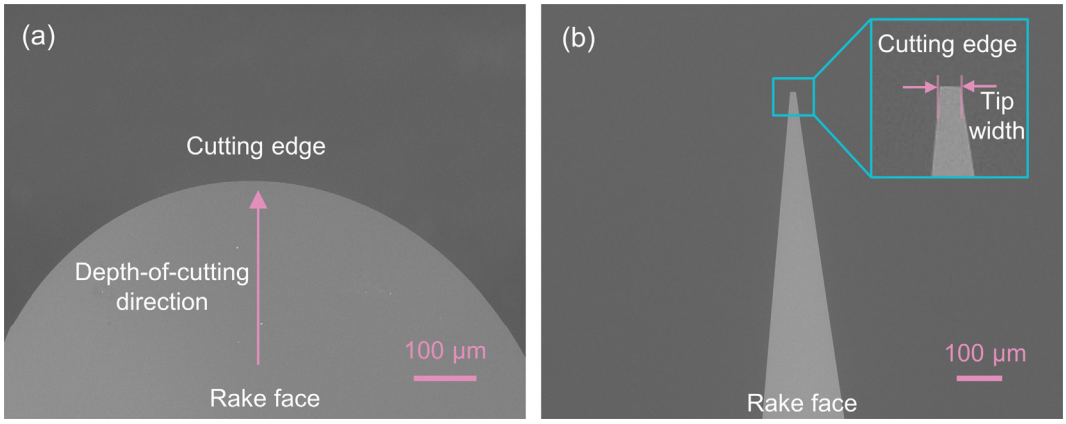

Fig. 1. Scanning electron microscope images of (a) the arc-shaped SCD cutting tool and (b) the trapezoid-shaped SCD cutting tool.

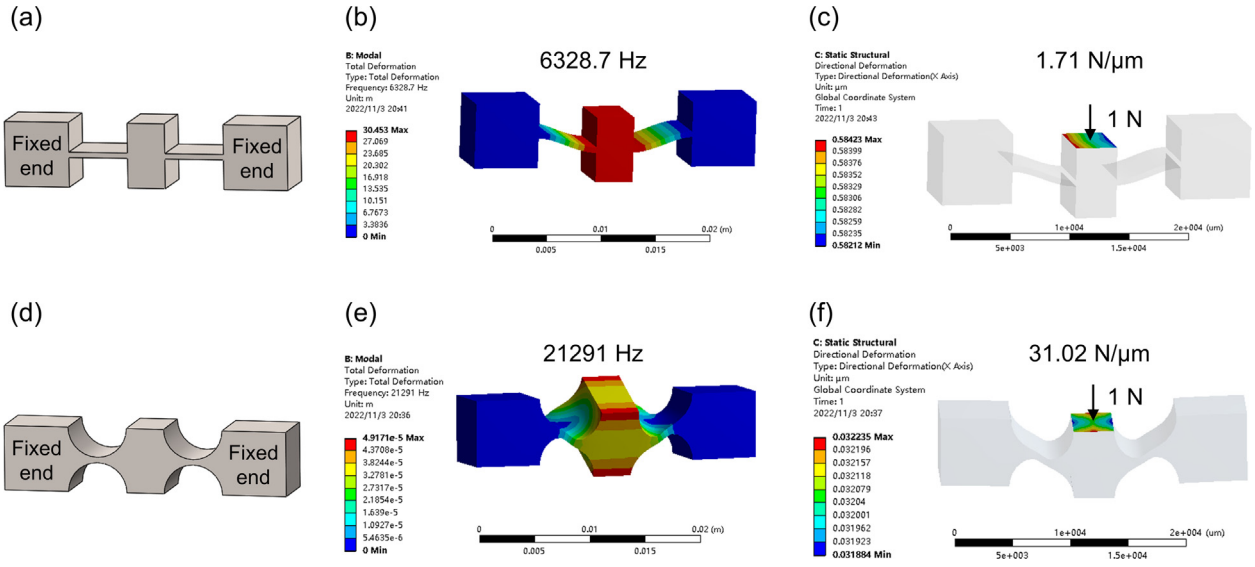

Fig. 2. (a) Three-dimensional model of the right-angle flexure hinge, (b) first-order resonant frequency of the right-angle flexure hinge, (c) stiffness of the right-angle flexure hinge, (d) three-dimensional model of the circular flexure hinge, (e) first-order resonant frequency of the circular flexure hinge, and (f) stiffness of the circular flexure hinge.

formance, which is chosen to transfer the original vibration motion from the piezoelectric actuator into the trapezoid-shaped SCD cutting tool.

Considering the assembly of the trapezoid-shaped SCD cutting tool and the piezoelectric actuator, a supporting structure with a symmetrical layout is designed, which avoids the undesired displacement disturbance along the depth-of-cutting direction during fabricating micro/nanostructure arrays. Besides, a supporting block with a square pit is chosen to fix the piezoelectric actuator. Integrating the circular flexure hinge with a supporting structure and a supporting block, the whole mechanical structure of the cutting system can be obtained, as illustrated in Fig. 3(a) and (b). The trapezoid-shaped SCD cutting tool and the piezoelectric actuator are located in the centreline of the mechanical structure. The trapezoid-shaped SCD cutting tool is fixed to the mechanical structure via the hex socket head bolt. The adjusting bolt is utilized to provide the piezoelectric actuator for the preload force.

The main working principle of the PA cutting system is, once the voltage signal (electrical signal) is inputted to the piezoelectric actuator then it generates the vibration motion (mechanical motion) by using the inverse piezoelectric effect. It is found that the inverse piezoelectric effect is the combination of the electrical signal and mechanical motion, so the PA cutting system is an electromechanically coupled system, which can be mathematically described by governing equations of piezoelectric materials [29]:

$$\rho \frac{D^2 d_i}{Dt^2} - \sigma_{ij,j} = \rho b_i \tag{1}$$

$$D_{i,i} = q \tag{2}$$

where ρ, d_i, σ_{ij}, b_i, D_i, and q are the density, displacement vector, the Cauchy stress tensor, body force vector, the electrical displacement vector, and the electric body charge, respectively. $\frac{D}{Dt}$ is the material derivative.

The constitutive equations are given to express the mathematical relation between the stress, strain, electric field, and electric displacement field in a strain-charge form or a stress-charge form [30]:

$$T_i = C_{ij}^E S_j - e_{ij} E_j \tag{3}$$

$$D_i = e_{ji} S_j + \varepsilon_{ij}^S E_j \tag{4}$$

$$S_i = s_{ij}^E T_j + d_{ij} E_j \tag{5}$$

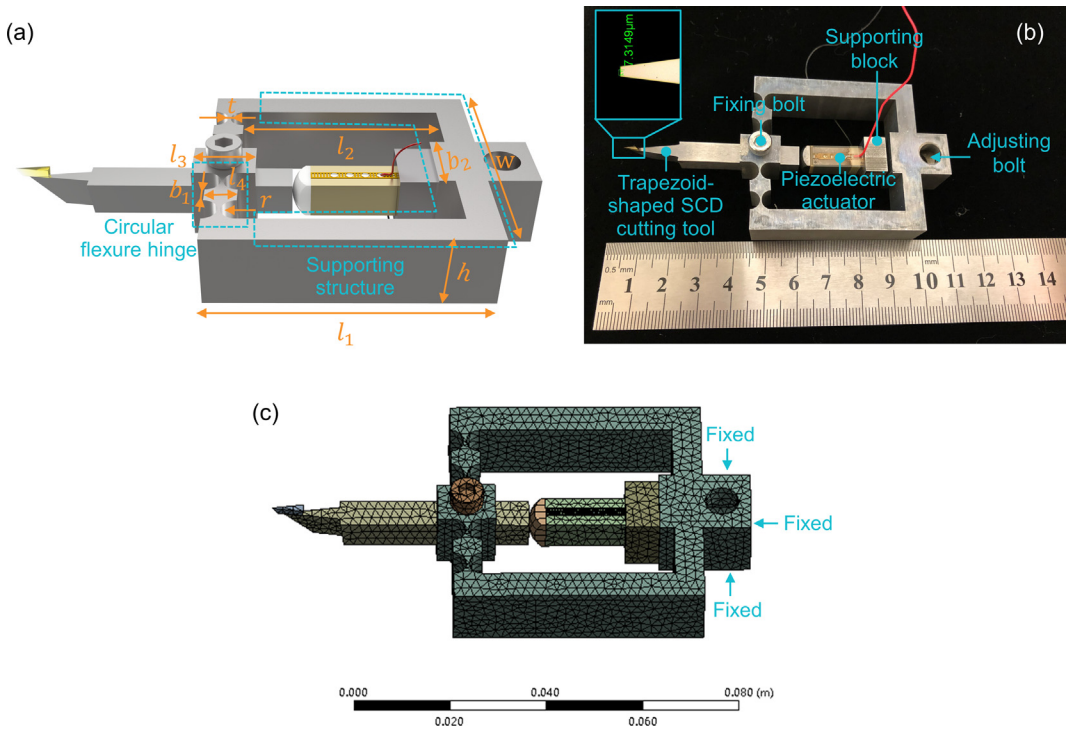

Fig. 3. (a) Three-dimensional model, (b) photograph, and (c) finite element model of the PA cutting system.

$$D_i = d_{ji}T_j + \varepsilon_{ij}^T E_j \tag{6}$$

where vectors T, S, E, and D are stress, strain, electric field, and electric displacement, respectively. The matrices C^E, e, s^E, d, ε^s, and ε^T are the mechanical stiffness at the constant electric field, the stress piezoelectric coefficient, the mechanical compliance at the constant electric field, the strain piezoelectric coefficient, the permittivity at constant strain, and the permittivity at constant stress, respectively. The subscript i, j = 1, 2, . . ., 6 refer to different directions within the piezoelectric material coordinate system. In this study, the material of the piezoelectric actuator is lead zirconate titanate.

Electrical discharge machining was used to manufacture the mechanical structure. The 304 stainless steel, due to its excellent durability and strength, was chosen as the material of the mechanical structure. The main sizes of the mechanical structure are summarized in Table 1.

3. Finite element analysis

The finite element simulation, as a high efficiency and visualization analysis method, was used to preliminary investigate the natural resonant frequencies and mode shapes of the PA cutting system. In general, the higher resonant frequency implies a wider working frequency area of the PA cutting system. A commercial software "ANSYS 19.0" was used to analyze the natural resonant frequencies and mode shapes, and the finite element model is shown in Fig. 3(c).

The mathematical model of the undamped system can be expressed in matrix notation:

$$[M]\{\ddot{u}\} + [K]\{u\} = \{0\} \tag{7}$$

where M is the mass matrix, $\ddot{u}$ is the 2nd time derivative of the displacement u, and K is the stiffness matrix.

Assume the displacement u is the harmonic motion:

$$\{u\} = \{\varnothing_i\}sin(\omega_i t) \tag{8}$$

where $\{\varnothing_i\}$ is the eigenvector representing the mode shape of the i^{th} natural circular frequency ω_i, and t is the time.

Then, the Eq. (7) becomes:

$$([K] - \omega_i^2[M])\{\varnothing_i\} = \{0\} \tag{9}$$

Next, the natural frequencies f_i can be obtained by solving Eq. (9):

$$f_i = \frac{\omega_i}{2\pi} \tag{10}$$

The three surfaces of the PA cutting system were fixed as the boundary conditions of the finite element model, as shown in Fig. 3(c). The contact type of the different components is the "bonded" type. And the material in the finite element model is 304 stainless steel. After these settings, simulation results of the finite element model can be obtained. Fig. 4 shows the simulation results of the first six-order resonant frequencies and mode shapes of the PA cutting system. The first-order resonant frequency of the PA cutting system is 1583.6 Hz, indicating that it has a wider working frequency area. The first-order mode shape is along the cutting direction. The second-order resonant frequency is 1630.7 Hz, and second-order mode shape is perpendicular to the rake face of the cutting tool. Similarly, other resonant frequencies and mode

Table 1
Main geometric sizes of the mechanical structure (sketched in Fig. 3(a), unit: mm).

w	h	r	t	l_1	l_2	l_3	l_4	b_1	b_2
50	14	2.75	0.5	52	40	12.05	6	3.5	14

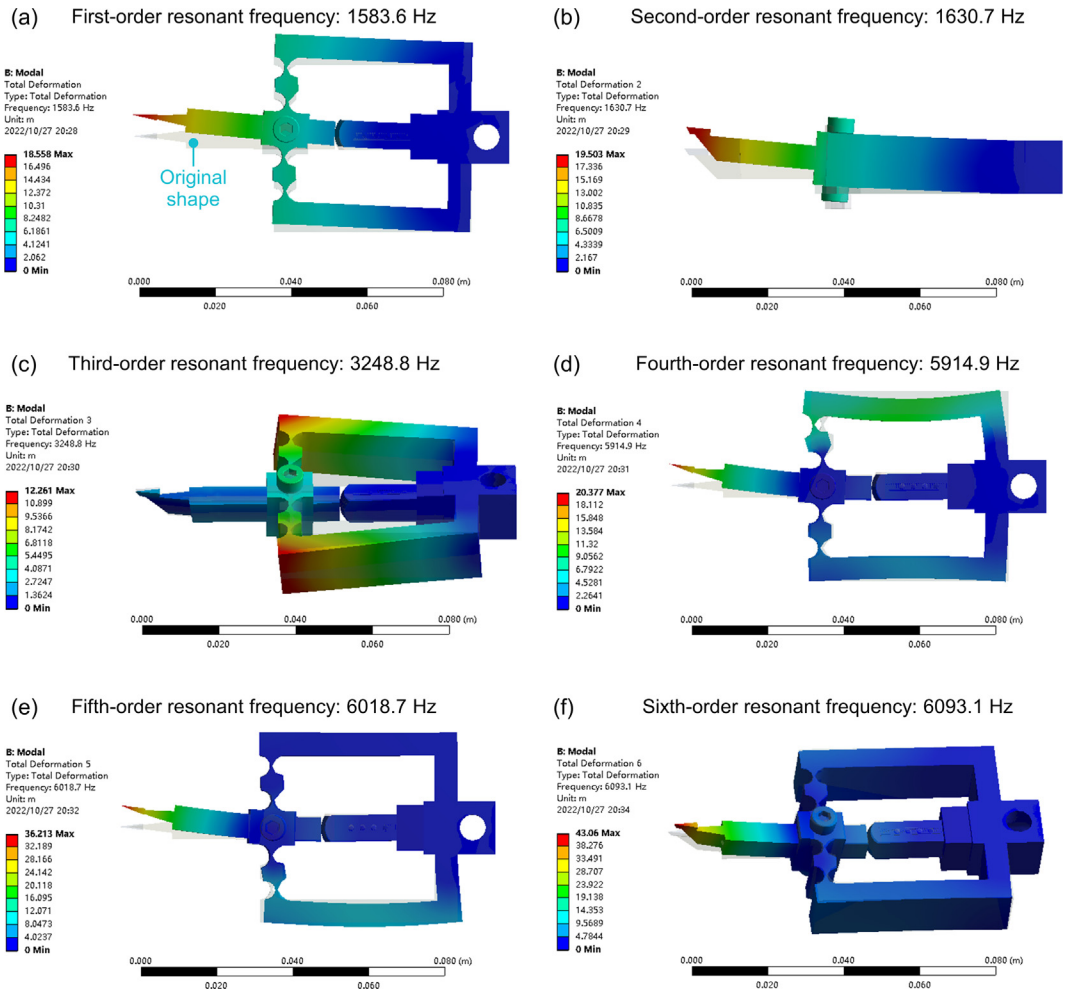

Fig. 4. The first six-order resonant frequencies and mode shapes of the PA cutting system. (a) First-order resonant frequency, (b) second-order resonant frequency, (c) third-order resonant frequency, (d) fourth-order resonant frequency, (e) fifth-order resonant frequency, and (f) sixth-order resonant frequency.

shapes can be observed. It can be found the different resonant frequencies of the PA cutting system have different mode shapes, which agrees with the vibration theory.

4. Experimental setup

4.1. Performance test experiments

During fabricating micro/nanostructure arrays, the maximum working frequency and maximum working stroke are significant performance specifications because the working frequency directly determines the fabrication efficiency, and the working stroke influences the height of the micro/nanostructure arrays. In general, the larger the working frequency, the higher the fabrication efficiency; the larger the working stroke, the larger the height of micro/nanostructure arrays. To determine these two specifications of the PA cutting system, a performance test platform was established, as shown in Fig. 5.

This performance test platform contained a personal computer, a high-sampling-rate multifunction I/O device, a high-performance piezo amplifier, and a capacitive displacement sensor. The computer offered the user interfaces and generated the digital signals by the software "LabVIEW". These command signals were digital signals. But the piezoelectric actuator (Physik Instrumente P-880.51, Germany) in the PA cutting system needed analogue signals (voltage signals). Therefore, a high- sampling-rate multifunction I/O device (National Instruments USB-6341, USA) was used to achieve the digital-to-analogue conversion. This device offered sixteen analogue input channels with a sampling rate of 500 kHz/s and two analogue output channels with a sample rate of 840 kHz/s, which met the requirement of performance tests of the PA cutting system. Besides, to meet the driving requirement of the piezoelectric actuator, a piezo amplifier by a factor of 10 (Physik Instrumente E-617, Germany) was used to magnify the analogue signals (voltage signals) in this platform. When the piezoelectric actuator received the voltage signals, the PA cutting system output the corresponding vibration motions. A capacitive displacement sensor with the root mean square (RMS) resolution of 5.99 nm and the measurement range of 500 μm (Elite, Lion Precision, USA) was used to ultra-precisely capture the output vibration motions at a sampling rate of 200 kHz. A swept frequency method was utilized to determine the maximum working frequency of the PA cutting system. The maximum working voltage (the peak-to-valley value is 100 V) was inputted to determine the maximum working stroke of the PA cutting system.

4.2. Fabrication experiments

An ultraprecision lathe (Moore Nanotech 350FG, Moore Tool Co., USA) was employed in fabricating high-aspect-ratio and hierarchical micro/nanostructure arrays, which offers the three linear motions in the X-, Y-, and Z-axis directions. The PA cutting system

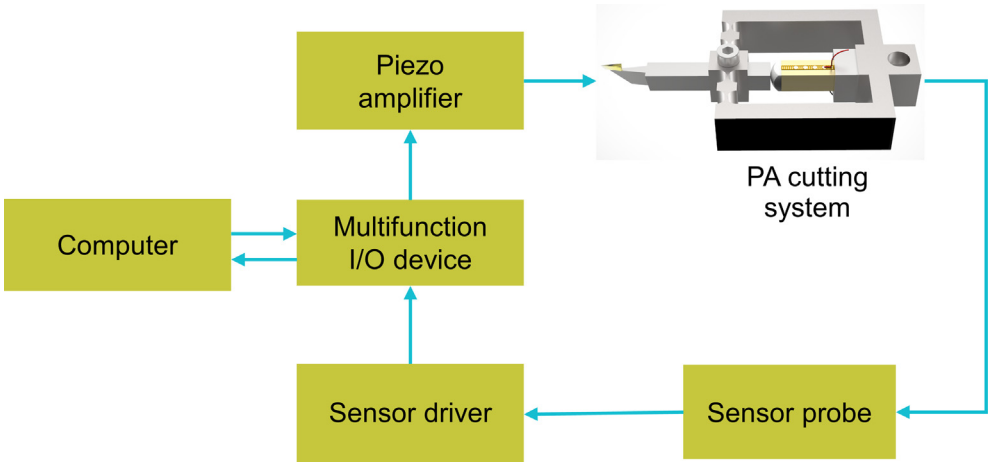

Fig. 5. Performance test platform of working performances of the PA cutting system.

was mounted on a micro height adjust tool holder. This micro height adjust tool holder was installed on the Z-axis of the Moore Nanotech 350FG, as presented in Fig. 6. The pure copper with 99.9 % purity was chosen as the workpiece material due to its better machinability. The material composition is listed in Table 2. The cuboid workpiece was installed on the spindle of the Moore Nanotech 350FG via a fixture. Before the fabrication of micro/nanostructure arrays, an arc-shaped SCD cutting tool was first used to flatten the original surface of the workpiece.

After flatting the workpiece surface, the trapezoid-shaped SCD cutting tool with a tip width of 7.3 μm (V70723, Contour Fine Tooling Inc., UK) was selected for generating high-aspect-ratio and hierarchical micro/nanostructures. The nominal cutting velocity, working frequency, and working voltage were set as 77.1 mm/min, 500 Hz, and 13 V, respectively.

5. Results and discussions

5.1. Working performances

The amplitude of the measured displacement was extracted and then the amplitude versus frequency was plotted, as shown in Fig. 7(a). It can be found that the amplitude shows a peak when the test frequency is 1510 Hz. This frequency is called the first-order resonant frequency. The error between the simulation result and the test result is 4.87 %, which demonstrates the effectiveness of the finite element model. It also shows the finite element analysis has a high simulation accuracy. Before the first-order resonance occurs, the amplitudes along the depth-of-cutting direction are very stable and the corresponding frequency range is 0 Hz ~ 1200 Hz, which is called the working frequency area of the PA cutting system. The amplitude slowly increases from 1200 Hz to 1510 Hz, which cannot be used during fabricating micro/nanostructure arrays because of its instability. Therefore,

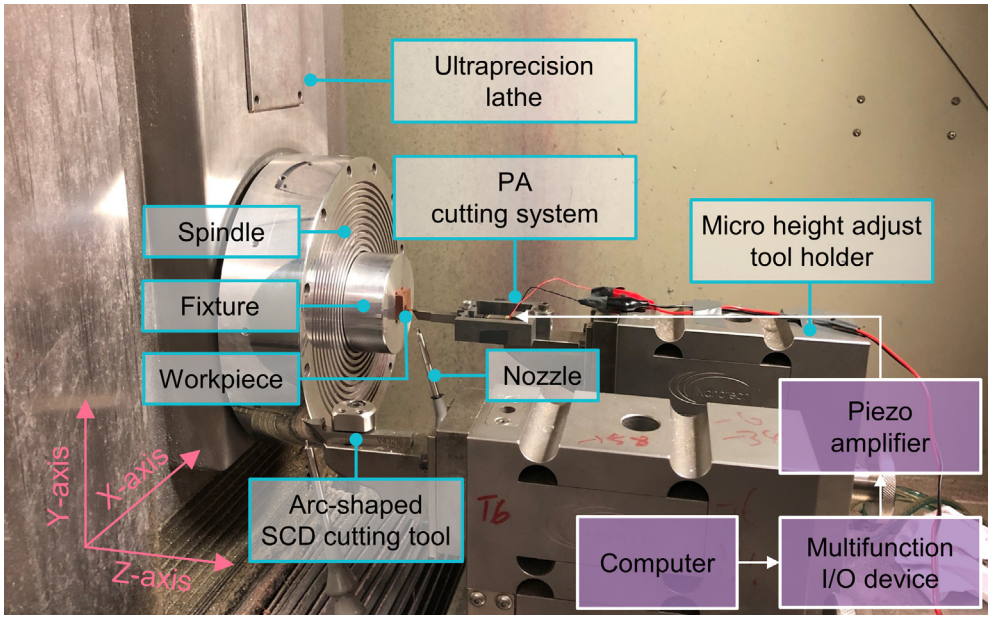

Fig. 6. The experimental setup of the micro/nanostructure array fabrication. The computer, multifunction I/O device, and piezo amplifier are located outside of the ultraprecision lathe, not observable in this figure.

Table 2
Material composition of the pure copper.

Cu	99.9 %									
Impurity elements (ppm)	Element	Zn	Se	Te	Bi	Cr	Mn	Sb	Cd	As	Co
	Content	0.3	0.4	0.4	0.5	0.6	0.3	1.0	0.1	0.3	1.5
	Element	P	Pb	S	Sn	Ni	Fe	Si	Ag	Others	
	Content	0.3	0.7	4.1	1.0	0.2	0.3	0.3	10.3	Bal.	

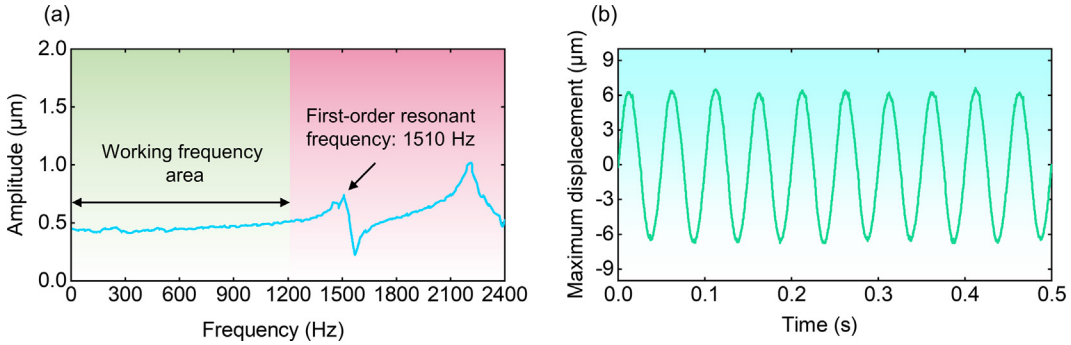

Fig. 7. Measurement results of working performances of the PA cutting system. (a) Maximum working frequency and (b) maximum displacement.

the maximum working frequency, as an important specification of the working performance, can be identified to be 1200 Hz.

Fig. 7(b) shows the maximum displacement when a sinusoidal voltage with a maximum amplitude of 50 V and a frequency of 20 Hz was inputted into the PA cutting system. The average peak and average valley of the maximum displacement are 6.34 μm and −6.72 μm. Therefore, the maximum working stroke is determined as 13.06 μm, which meets the normal requirements of fabricating micro/nanostructure arrays.

5.2. Characterization of micro/nanostructure arrays

After the diamond turning (flatting) of the original surface, a mirror surface can be obtained, as shown in Fig. 8(a). A clear picture (a cartoon sticker) on the sample surface can be viewed clearly because of the low surface roughness. For quantitatively acquiring the values of the surface roughness, a white light interferometer (Nexview™, Zygo Corp., USA) was used, which has a sub-nanometre precision and the capability of realizing faster measurements. Fig. 8(b)-(d) show measured results of the surface roughness (R_a) at the three different regions of this mirror surface. The average value is 2.33 nm, which achieves ultraprecision fabrication and provides an ultra-good surface before fabricating high-aspect-ratio and hierarchical micro/nanostructure arrays.

Fig. 9 presents the morphologies of the micro/nanostructure array that was fabricated by the PA cutting system. It can be found that the micro/nanostructures array has the high-aspect-ratio and the multilayer. The number (n) can be used to define the number of layers of micro/nanostructure arrays [31]. For n = 0, there is not any micro/nanostructure array. n = 1 presents that there is a one-layer micro/nanostructure array on the workpiece surface, and so forth. In this preliminary fabrication experiment (named "Case 1"), n = 2 because the two-layer micro/nanostructure array is fabricated on the workpiece surface, as demonstrated in Fig. 9(a) and (b). The first layer is the micro-groove array. The direction of the micro-groove array is parallel with the cutting direction (Y-axis direction, as described in Fig. 6). The second layer is the nano-groove array, and its direction is perpendicular to the cutting direction (X-axis direction). The cross-sectional profile of the micro-groove array is plotted in Fig. 9(c). It can be observed that the micro-groove array has a right-angle cross-sectional profile. According to the average values of the height h of the micro-groove array and the width w, the aspect ratio ($r = h/w$) is calculated as 0.28. If using an act-shaped SCD cutting tool with a 0.5 mm radius to machine the same height (9.27 μm), the aspect ratio is 0.097. Therefore, in comparison to the conventional mechanical cutting system [32], the PA cutting system increases the aspect ratio by 188.7 %.

Fig. 9(d) plots the cross-sectional profile of the nano-groove array. It has a steep triangle profile with a height of 265 nm and a spacing of 2.71 μm. The design value of the spacing is 2.57 μm, which is calculated by fabrication parameters (the spacing is the ratio of the nominal cutting velocity over the working frequency of the PA cutting system). Therefore, the fabrication error about the spacing of the nano-groove array is 5.06 %. For the micro/-nanoscale fabrication, it is a very low fabrication error because when the size decreases to the microscale or nanoscale, many factors influence the fabrication error, such as the material elastic recovery, inhomogeneous grain size, assembly error, cutting tool wear, and external disturbance of the fabrication environment, and so on.

To further demonstrate the effectiveness and flexibility of the PA cutting system, another two kinds of micro/nanostructure arrays were fabricated, named "Case 2" and "Case 3". Fig. 10 presents the three-dimensional morphologies and cross-sectional profile of Case 2. Different from Case 1, the second layer is the sine-shaped microstructure array. For Case 3, both the first layer and the second layer have sine-shaped cross-sectional profiles, as presented in Fig. 11, which further shows the flexibility of the PA cutting system.

5.3. Corrosion property of fabricated micro/nanostructure arrays

To explore the function of the fabricated micro/nanostructure arrays, the corrosion property was studied by using the electrochemical workstation (Interface 1000™, Gamry Instruments, USA) at the room temperature. Fig. 12 presents the potentiodynamic polarization curves of the mirror surface and fabricated micro/-nanostructure array surface (Case 1) in the 3.5 wt% NaCl solution. It can be found that potentiodynamic polarization curves of the mirror surface and micro/nanostructure array surface are very close. In order to quantitatively analyze their differences, the corrosion potential (E_{corr}) and corrosion current density (I_{corr}) are

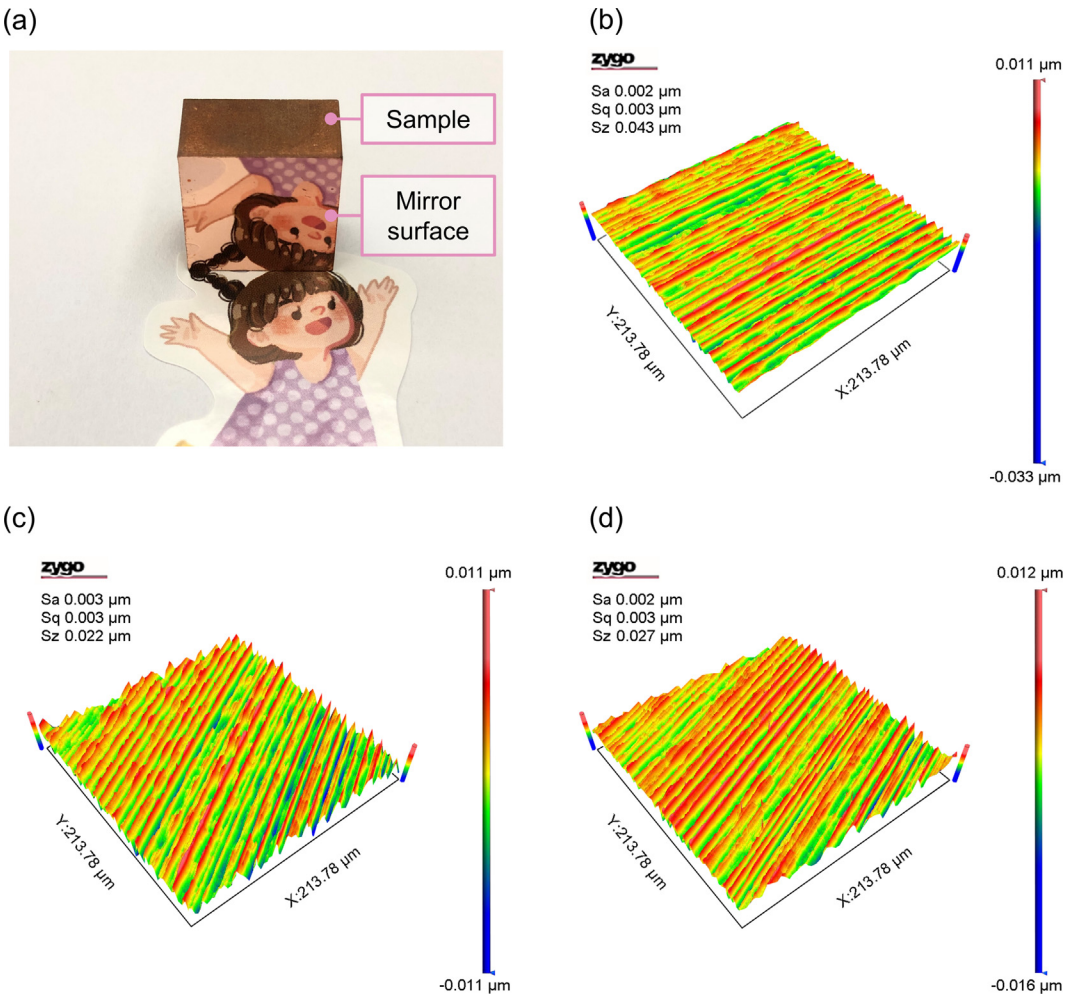

Fig. 8. (a) Photograph of the mirror surface and (b)-(d) surface roughness at different measurement regions of the mirror surface.

extracted from potentiodynamic polarization curves by using the Tafel extrapolation method, and they are listed in Table 3. In general, the higher $-E_{corr}$ and lower I_{corr} mean the better corrosion resistance [33,34]. It is observed that the micro/nanostructure array surface causes the improvement in $-E_{corr}$ and the reduction in I_{corr}, which confirms that the micro/nanostructure array surface has better corrosion resistance. The corrosion inhibition efficiency can be calculated by the following equation [35,36]:

$$\eta = \frac{I_{corr(0)} - I_{corr(i)}}{I_{corr(0)}} \times 100\% \tag{11}$$

where $I_{corr(0)}$ is the corrosion current of the mirror surface and $I_{corr(i)}$ is the corrosion current of the micro/nanostructure array surface.

The corrosion inhibition efficiency η of the micro/nanostructure array surface is 18.5 %, which shows the micro/nanostructure array on the pure copper surface acts as a protective film to improve the corrosion resistance of the raw materials [37–39].

6. Conclusions

In this study, a novel piezoelectrically actuated (PA) cutting system is designed for fabricating high-aspect-ratio and hierarchical micro/nanostructure arrays on metal surfaces. The mechanical design, finite element analysis, performance test, and micro/nanostructure array fabrication were systematically performed. The main conclusions of this study are as follows:

1) The mechanical structure of the PA cutting system was designed based on the circular flexure hinge, and the symmetrical arrangement helped to reduce external disturbances. In the PA cutting system, a trapezoid-shaped signal-crystal-diamond cutting tool was used for increasing the aspect ratio of micro/nanostructure arrays. And a piezoelectric actuator was used for increasing the layers of micro/nanostructure arrays by adding the high-order vibration motion to the cutting tool.
2) A performance test platform was established to accurately determine the performance specifications of the PA cutting system. The maximum working frequency and maximum working stroke were 1200 Hz and 13.06 μm, respectively, demonstrating superior performances of the PA cutting system.
3) Various two-layer micro/nanostructure arrays with low fabrication error were successfully fabricated on pure copper surfaces. These micro/nanostructure arrays had two characteristics: high aspect ratio and multilayer. Compared with conventional mechanical cutting systems, the PA cutting system increased the aspect ratio of micro/nanostructure arrays by 188.7 %, demonstrating the effectiveness of the PA cutting system.

Besides, the fabricated micro/nanostructure arrays improved the corrosion resistance of the raw material by 18.5 %. This finding

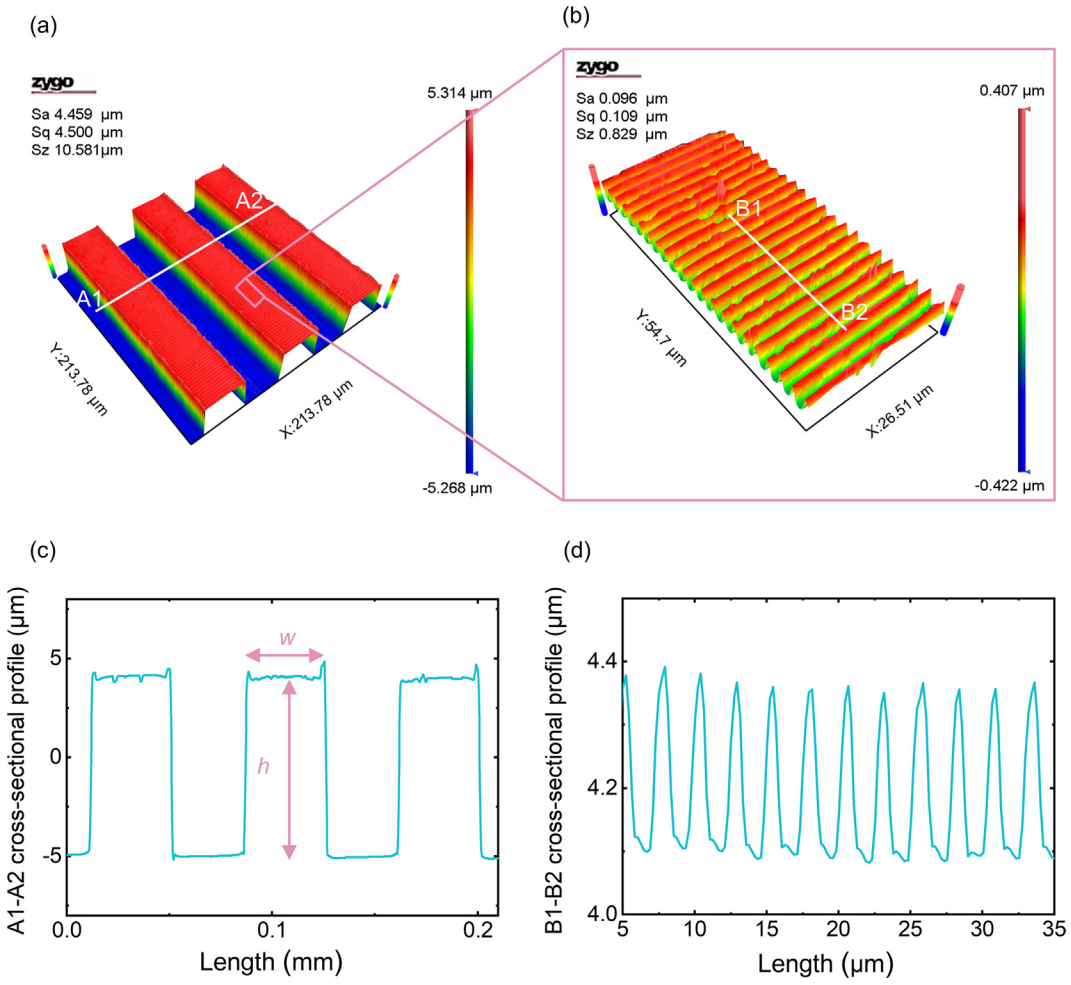

Fig. 9. (a and b) Morphologies and (c and d) cross-sectional profiles of the high-aspect-ratio and hierarchical micro/nanostructure array in Case 1.

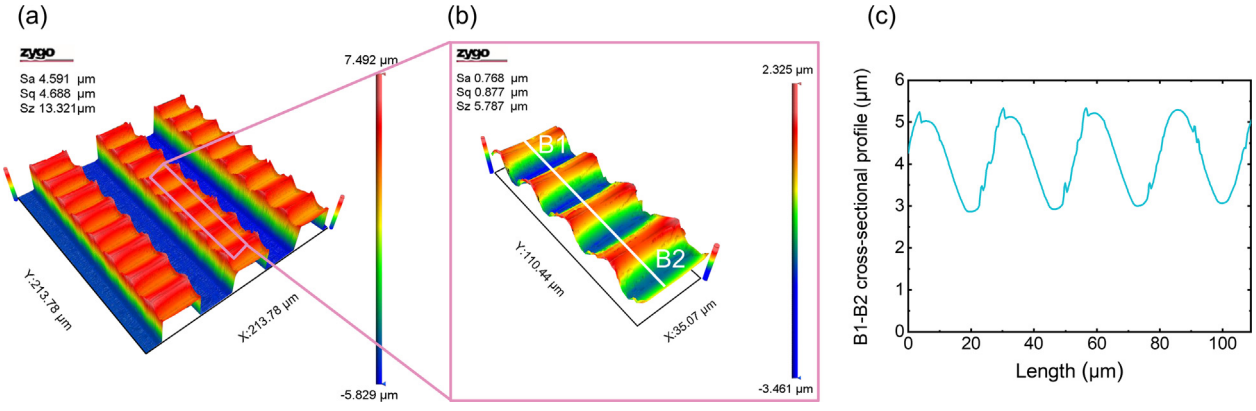

Fig. 10. (a and b) Morphologies and (c) cross-sectional profile of the high-aspect-ratio and hierarchical micro/nanostructure array in Case 2.

could be applied in pipeline and ship industries for reducing corrosion in the future.

CRediT authorship contribution statement

Hanheng Du: Conceptualization, Methodology, Software, Validation, Formal analysis, Investigation, Data curation, Writing - original draft, Writing - review & editing. **Zhiwei Zhu:** Supervision. **Zuankai Wang:** Supervision. **Suet To:** Supervision, Funding acquisition.

Data availability

Data will be made available on request.

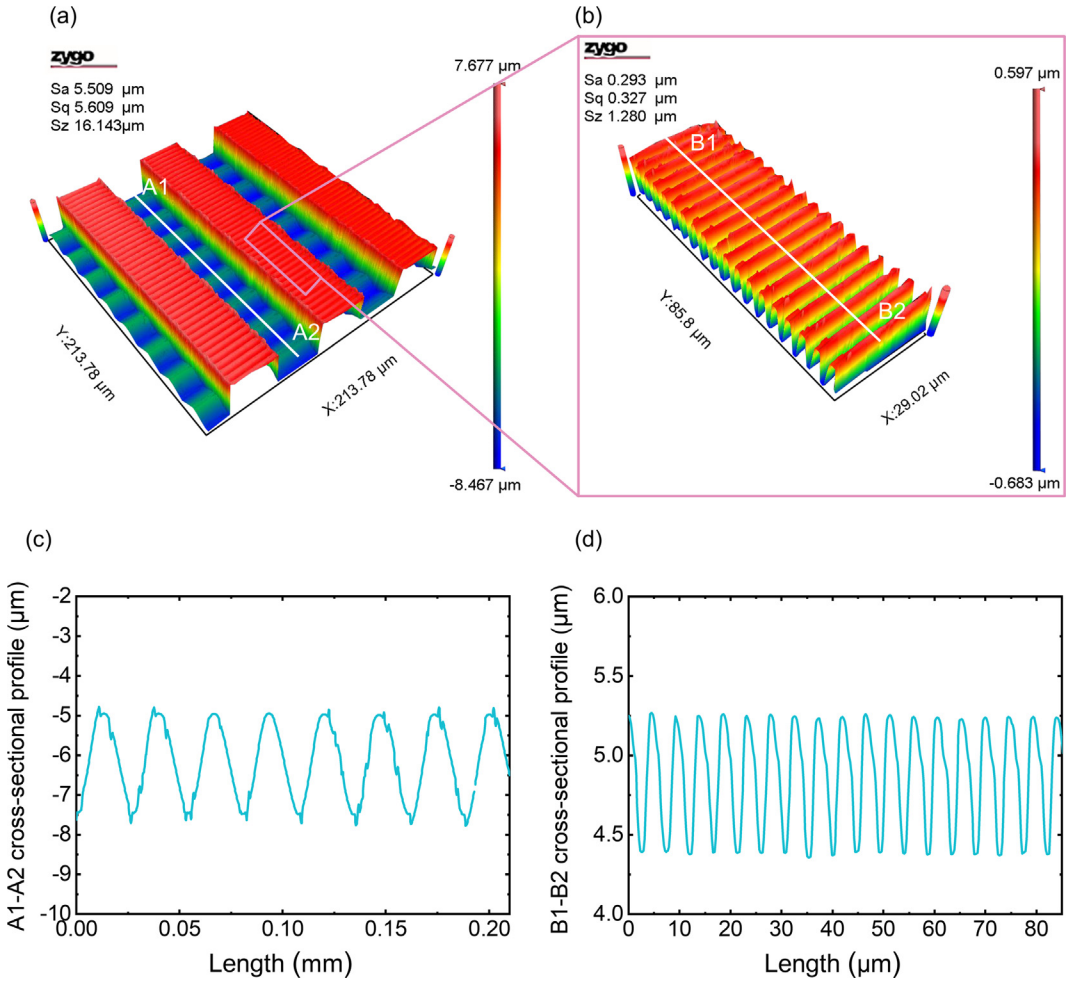

Fig. 11. (a and b) Morphologies and (c and d) cross-sectional profiles of the high-aspect-ratio and hierarchical micro/nanostructure array in Case 3.

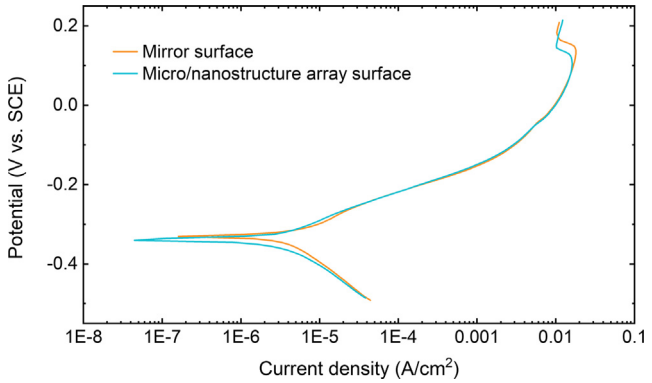

Fig. 12. Potentiodynamic polarization curves of the mirror surface and micro/nanostructure array surface. The corrosion inhibition efficiency of machined micro/nanostructure array can be obtained using the potentiodynamic polarization curve.

Table 3
Polarization curve parameters of the mirror surface and micro/nanostructure array surface.

Samples	E_{corr} (V vs SCE)	I_{corr} (A/cm^2)
Mirror surface	−0.332	3.25×10^{-6}
Micro/nanostructure array surface	−0.339	2.65×10^{-6}

Declaration of Competing Interest

The authors declare that they have no known competing financial interests or personal relationships that could have appeared to influence the work reported in this paper.

Acknowledgement

This work was funded by the Research Grants Council of the Hong Kong Special Administrative Region, China (Project No.: PolyU 15221322), the National Natural Science Foundation of China (Project No.: U19A20104), and State Key Laboratory of Ultra-precision Machining Technology.

References

[1] Y. Xiao, J. Huang, Z. Guo, W. Liu, Nanotree array textured lubricant-infused frame for efficient fog harvesting, Materials Today Physics. 28 (2022), https://doi.org/10.1016/J.MTPHYS.2022.100869 100869.
[2] Y. Sun, Y. Zheng, R. Wang, T. Lei, J. Liu, J. Fan, W. Shou, Y. Liu, 3D micro-nanostructure based waterproof triboelectric nanogenerator as an outdoor adventure power source, Nano Energy 100 (2022), https://doi.org/10.1016/j.nanoen.2022.107506 107506.
[3] A. Ramesh, W. Akram, S.P. Mishra, A.H. Cannon, A.A. Polycarpou, W.P. King, Friction characteristics of microtextured surfaces under mixed and hydrodynamic lubrication, Tribol. Int. 57 (2013) 170–176, https://doi.org/10.1016/j.triboint.2012.07.020.
[4] J.J. Brandner, E. Anurjew, L. Bohn, E. Hansjosten, T. Henning, U. Schygulla, A. Wenka, K. Schubert, Concepts and realization of microstructure heat exchangers for enhanced heat transfer, Exp. Therm Fluid Sci. 30 (2006) 801–809, https://doi.org/10.1016/j.expthermflusci.2006.03.009.

[5] H. Chen, L. Zhang, P. Zhang, D. Zhang, Z. Han, L. Jiang, A Novel Bioinspired Continuous Unidirectional Liquid Spreading Surface Structure from the Peristome Surface of Nepenthes alata, Small 13 (2017) 1–6, https://doi.org/10.1002/smll.201601676.
[6] Y.W. Su, C.S. Wu, C.C. Chen, C.D. Chen, Fabrication of two-dimensional arrays of CdSe pillars using E-beam lithography and electrochemical deposition, Adv. Mater. 15 (2003) 49–51, https://doi.org/10.1002/adma.200390008.
[7] Z. Faraji Rad, P.D. Prewett, G.J. Davies, High-resolution two-photon polymerization: the most versatile technique for the fabrication of microneedle arrays, Microsyst. Nanoeng. 7 (2021), https://doi.org/10.1038/s41378-021-00298-3.
[8] C. Hahn, A. Hajebifard, P. Berini, Helium focused ion beam direct milling of plasmonic heptamer-arranged nanohole arrays, Nanophotonics. 9 (2020) 393–399, https://doi.org/10.1515/nanoph-2019-0385.
[9] D.M. Chun, C.V. Ngo, K.M. Lee, Fast fabrication of superhydrophobic metallic surface using nanosecond laser texturing and low-temperature annealing, CIRP Ann. Manuf. Technol. 65 (2016) 519–522, https://doi.org/10.1016/j.cirp.2016.04.019.
[10] H. Yu, J. Han, S. Li, D. Zhao, J. Wang, Y. Tian, J. Lin, Hierachical micro/nano structures fabrication by a novel tri-axial piezoelectric servo system, Mater. Des. 224 (2022), https://doi.org/10.1016/j.matdes.2022.111330 111330.
[11] Z. Zhu, S. To, S. Zhang, Active control of residual tool marks for freeform optics functionalization by novel biaxial servo assisted fly cutting, Appl. Opt. 54 (2015) 7656, https://doi.org/10.1364/ao.54.007656.
[12] T. Zhou, J. Zhou, T. Wang, L. Gao, B. Ruan, Q. Yu, W. Zhao, X. Wang, Fabrication of high aspect-ratio aspheric microlens array based on local spiral diamond milling, J. Manuf. Process. 83 (2022) 547–554, https://doi.org/10.1016/J.JMAPRO.2022.08.064.
[13] A. Meier, Diamond turning of diffractive microstructures, Precis. Eng. 42 (2015) 253–260, https://doi.org/10.1016/j.precisioneng.2015.05.007.
[14] P. Guo, K.F. Ehmann, An analysis of the surface generation mechanics of the elliptical vibration texturing process, Int. J. Mach. Tool Manu. 64 (2013) 85–95, https://doi.org/10.1016/j.ijmachtools.2012.08.003.
[15] Y. He, T. Zhou, X. Dong, P. Liu, W. Zhao, X. Wang, Y. Hu, J. Yan, Generation of high-saturation two-level iridescent structures by vibration-assisted fly cutting, Mater. Des. 193 (2020), https://doi.org/10.1016/j.matdes.2020.108839 108839.
[16] S.A. Sajjady, H. Nouri Hossein Abadi, S. Amini, R. Nosouhi, Analytical and experimental study of topography of surface texture in ultrasonic vibration assisted turning, Mater Des. 93 (2016), 311–323. 10.1016/j.matdes.2015.12.119.
[17] N. Suzuki, H. Yokoi, E. Shamoto, Micro/nano sculpturing of hardened steel by controlling vibration amplitude in elliptical vibration cutting, Precis. Eng. 35 (2011) 44–50, https://doi.org/10.1016/j.precisioneng.2010.09.006.
[18] P. Guo, K.F. Ehmann, Development of a tertiary motion generator for elliptical vibration texturing, Precis. Eng. 37 (2013) 364–371, https://doi.org/10.1016/j.precisioneng.2012.10.005.
[19] Z. Zhu, H. Du, R. Zhou, P. Huang, W. le Zhu, P. Guo, Design and trajectory tracking of a nanometric ultra-fast tool servo, IEEE Trans. Ind. Electron. 67 (2020) 432–441, https://doi.org/10.1109/TIE.2019.2896103.
[20] Z.H. Zhu, L. Chen, Y. Niu, X. Pu, P. Huang, S. To, L. Zhu, Z. Zhu, Tri-axial Fast Tool Servo Using Hybrid Electromagnetic-Piezoelectric Actuation for Diamond Turning, IEEE Trans. Ind. Electron. 69 (2021) 1728–1738, https://doi.org/10.1109/TIE.2021.3060635.
[21] H. Du, S. To, W. Sze Yip, Z. Zhu, Development and assessment of a novel two-degree-of-freedom vibration generator for generating and hiding optical information, Mech. Syst. Sig. Process. 181 (2022), https://doi.org/10.1016/J.YMSSP.2022.109470 109470.
[22] Y. Wan, Z. Qiu, Y. Hong, Y. Wang, J. Zhang, Q. Liu, Z. Wu, C.F. Guo, A Highly Sensitive Flexible Capacitive Tactile Sensor with Sparse and High-Aspect-Ratio Microstructures, Adv. Electron. Mater. 4 (2018), https://doi.org/10.1002/aelm.201700586.
[23] Y. Liu, L. Moevius, X. Xu, T. Qian, J.M. Yeomans, Z. Wang, Pancake bouncing on superhydrophobic surfaces, Nat. Phys. 10 (2014) 515–519, https://doi.org/10.1038/nphys2980.
[24] G. Chen, B. Ji, Y. Gao, C. Wang, J. Wu, B. Zhou, W. Wen, Towards the rapid and efficient mixing on "open-surface" droplet-based microfluidics via magnetic actuation, Sens Actuators B Chem. 286 (2019) 181–190, https://doi.org/10.1016/j.snb.2019.01.126.
[25] P. Kim, W.E. Adorno-Martinez, M. Khan, J. Aizenberg, Enriching libraries of high-aspect-ratio micro-or nanostructures by rapid, low-cost, benchtop nanofabrication, Nat. Protoc. 7 (2012) 311–327, https://doi.org/10.1038/nprot.2012.003.
[26] Y.P. Lin, Y. Zhang, M.F. Yu, Parallel Process 3D Metal Microprinting, Adv Mater Technol. 4 (2019), https://doi.org/10.1002/admt.201800393.
[27] Q. Zhang, J. Zhao, Y. Peng, H. Pu, Y. Yang, A novel amplification ratio model of a decoupled XY precision positioning stage combined with elastic beam theory and Castigliano's second theorem considering the exact loading force, Mech. Syst. Sig. Process. 136 (2020), https://doi.org/10.1016/j.ymssp.2019.106473 106473.
[28] F. Chen, Q. Zhang, W. Dong, L. Sun, Design and test of a compact large-stroke dual-drive linear-motion system, Mech. Syst. Sig. Process. 180 (2022), https://doi.org/10.1016/j.ymssp.2022.109438 109438.
[29] S. Kaneko, G. Hong, N. Mitsume, T. Yamada, S. Yoshimura, Numerical study of active control by piezoelectric materials for fluid–structure interaction problems, J. Sound Vib. 435 (2018) 23–35, https://doi.org/10.1016/j.jsv.2018.07.044.
[30] E. Elka, D. Elata, H. Abramovich, The electromechanical response of multilayered piezoelectric structures, J. Microelectromech. Syst. 13 (2004) 332–341, https://doi.org/10.1109/JMEMS.2004.825307.
[31] R.S. Lokes, Materials with structural hierarchy, Nature 361 (511–15) (1993) 511–515. https://www.nature.com/articles/361511a0.pdf.
[32] H. Du, W. Yip, Z. Zhu, S. To, Development of a two-degree-of-freedom vibration generator for fabricating optical microstructure arrays, Opt. Express 29 (2021) 25903–25921.
[33] L. Yang, Y. Wan, Z. Qin, Q. Xu, Y. Min, Fabrication and corrosion resistance of a graphene-tin oxide composite film on aluminium alloy 6061, Corros. Sci. 130 (2018) 85–94, https://doi.org/10.1016/j.corsci.2017.10.031.
[34] S. Shen, C. di Zhu, X.Y. Guo, C.C. Li, Y. Wen, H.F. Yang, The synergistic mechanism of phytic acid monolayers and iodide ions for inhibition of copper corrosion in acidic media, RSC Adv. 4 (2014) 10597–10606, https://doi.org/10.1039/c3ra47291d.
[35] M.A. Deyab, Electrochemical investigations on pitting corrosion inhibition of mild steel by provitamin B5 in circulating cooling water, Electrochim. Acta 202 (2016) 262–268, https://doi.org/10.1016/j.electacta.2015.11.075.
[36] Z. Hu, F. Ma, L. Shen, B. Zhu, J. Yi, Z. Zeng, Q. Li, Superior anti-corrosion performance on Cu substrate achieved by dense polypropylene coating with ultrahigh inhibition efficiency deposited via the environmental-friendly method, Corros. Sci. 191 (2021), https://doi.org/10.1016/j.corsci.2021.109783 109783.
[37] Z. Sharifalhoseini, M.H. Entezari, A. Davoodi, M. Shahidi, Access to nanocrystalline, uniform, and fine-grained Ni-P coating with improved anticorrosive action through the growth of ZnO nanostructures before the plating process, Corros. Sci. 172 (2020), https://doi.org/10.1016/J.CORSCI.2020.108743 108743.
[38] G. Wang, Y. Shen, J. Tao, X. Luo, M. Jin, Y. Xie, Z. Li, S. Guo, Facilely constructing micro-nanostructure superhydrophobic aluminum surface with robust ice-phobicity and corrosion resistance, Surf. Coat. Technol. 329 (2017) 224–231, https://doi.org/10.1016/J.SURFCOAT.2017.09.055.
[39] B. Park, W. Hwang, A facile fabrication method for corrosion-resistant micro/nanostructures on stainless steel surfaces with tunable wettability, Scr. Mater. 113 (2016) 118–121, https://doi.org/10.1016/J.SCRIPTAMAT.2015.10.018.